

## Article

# Effect of Sr Deficiency on Electrical Conductivity of Yb-Doped Strontium Zirconate

Adelya Khaliullina , Anastasia Meshcherskikh , Aleksander Pankratov and Liliya Dunyushkina \* 

Institute of High Temperature Electrochemistry, 20 Akademicheskaya St., 620990 Ekaterinburg, Russia; adelia01@mail.ru (A.K.); lazyty@mail.ru (A.M.); a.pankratov@ihte.uran.ru (A.P.)

\* Correspondence: lidung@list.ru; Tel.: +73-433-623-240

**Abstract:** The effect of Sr-deficiency on microstructure, phase composition and electrical conductivity of  $\text{Sr}_x\text{Zr}_{0.95}\text{Yb}_{0.05}\text{O}_{3-\delta}$  ( $x = 0.94\text{--}1.00$ ) was investigated via X-ray diffraction, scanning electron microscopy, energy-dispersive X-ray spectroscopy and impedance spectroscopy. The samples were synthesized by a chemical solution method and sintered at 1600 °C. According to X-ray diffraction data, the samples with  $x = 0.96\text{--}1.00$  were single-phase oxides possessing an orthorhombic perovskite-type structure; while zirconia-based minor phases arise at  $x = 0.94$ , which was confirmed by the electron microscopy. Sr stoichiometry was shown to influence the electrical conductivity. The highest total and bulk conductivities,  $6\text{--}10^{-4}\text{ Scm}^{-1}$  and  $3\text{--}10^{-3}\text{ Scm}^{-1}$ , respectively, at 600 °C in humid air ( $p\text{H}_2\text{O} = 3.2\text{ kPa}$ ), were observed for the  $x = 0.98$  composition. In the temperature range of 300–600 °C, the conductivity of the samples with  $x = 0.96\text{--}1.00$  increased with the increase in humidity, which indicates a significant contribution of protonic defects to the charge transport. Electrical conductivity of  $\text{Sr}_x\text{Zr}_{0.95}\text{Yb}_{0.05}\text{O}_{3-\delta}$  was discussed in terms of the defect formation model and the secondary phases precipitation.

**Keywords:** Yb-doped strontium zirconate; strontium stoichiometry; conductivity; proton conduction



**Citation:** Khaliullina, A.; Meshcherskikh, A.; Pankratov, A.; Dunyushkina, L. Effect of Sr Deficiency on Electrical Conductivity of Yb-Doped Strontium Zirconate. *Materials* **2022**, *15*, 4126. <https://doi.org/10.3390/ma15124126>

Academic Editor: Philippe Colombar

Received: 13 May 2022

Accepted: 8 June 2022

Published: 10 June 2022

**Publisher's Note:** MDPI stays neutral with regard to jurisdictional claims in published maps and institutional affiliations.



**Copyright:** © 2022 by the authors. Licensee MDPI, Basel, Switzerland. This article is an open access article distributed under the terms and conditions of the Creative Commons Attribution (CC BY) license (<https://creativecommons.org/licenses/by/4.0/>).

## 1. Introduction

Ceramic oxides exhibiting high oxide-ion and proton conductivity at the intermediate temperatures are of considerable interest for application as solid electrolytes in clean energy technologies. Proton-conducting solid oxide fuel cells (PC-SOFCs) have great potential for clean energy production by conversion of fuel chemical energy into electricity. Water splitting by using solid oxide electrolysis cells (SOECs) is a promising technology for the production of clean hydrogen which is currently considered as the fuel of the future. Proton-conducting SOFCs and SOECs operate at lower temperatures compared to the traditional oxide-ion conducting cells due to the high proton mobility. Proton conducting membranes are required to possess excellent ionic conductivity, as low as possible electronic conductivity, and chemical stability in oxidizing and reducing conditions, in order to provide high performance of the energy/fuel conversion and storage systems.

Alkaline-earth cerates and zirconates with a perovskite structure have been found to exhibit appreciable proton conduction in humid atmospheres in the intermediate temperature range (300–700 °C) [1–9]. Acceptor-doped barium and strontium cerates possess the highest proton conductivity among  $\text{ABO}_3$  perovskites; however, their poor chemical stability in atmospheres containing carbon and sulfur oxides, which is manifested in the formation of barium carbonate (sulfate) and  $\text{CeO}_2$ -based oxides, hinders their practical use [1,7,10,11]. Thus, zirconates of strontium and barium, exhibiting lower proton conductivity, but higher chemical stability compared to the cerates, are considered as alternative candidates for the proton-conducting membranes of the solid oxide cells.

The study of the processes of hydration of the alkaline-earth zirconates [12,13], hydrogen isotope distribution, hydrogen solubility and diffusivity [14,15], the isotope effect on

the electrical conductivity [16], and the effect of the water vapor partial pressure on the conductivity [4–6,17–19] regardless of certain differences, proved the proton incorporation and participation in the charge transport process in the perovskites. As demonstrated by multiple studies, the ionic ( $O^{2-}$  and  $H^+$ ) conductivity of the zirconates can be improved by substitution of zirconium with trivalent cations that promote the generation of oxygen vacancies to maintain charge balance, see e.g., [4–8,18,19].

Along with the acceptor doping, A-site stoichiometry was shown to influence the conducting behavior of  $ABO_3$  perovskites ( $A = Sr, Ba$ ;  $B = Zr, Ce$ ) [11,17,19–21]. Recently, we have reported that  $Sr_{0.98}Zr_{0.95}Y_{0.05}O_{3-\delta}$  composition exhibited the highest ionic conductivity among  $Sr_xZr_{0.95}Y_{0.05}O_{3-\delta}$  ( $x = 0.94–1.02$ ) series [19], which was interpreted as follows. A-site deficiency promotes the generation of additional oxygen vacancies that result in a rise of ionic conductivity; but on the other hand, it boosts the placement of the dopant ions into A-sites instead of B-sites. In A-sites, the trivalent cation acts as a donor impurity, which leads to a decrease in the oxygen vacancy concentration. As a result of these two opposite processes, the dependence of conductivity on Sr content has a maximum point at  $x = 0.98$ .

Yb-doped  $SrZrO_3$  was reported to possess a higher electrical conductivity compared to the Y-, Sc-, Er-, In-, Al- and Ga-doped strontium zirconates [5,6], which makes it more attractive for practical use. The solubility limit of ytterbium in  $SrZr_{1-x}Yb_xO_{3-\delta}$  was reported to be about 5 at. %, and the conductivity was shown to increase with an increase in Yb concentration, reaching a maximal value for the  $SrZr_{0.95}Yb_{0.05}O_{3-\delta}$  composition [22]. However, to the best of our knowledge, the influence of Sr content on the conducting properties of this perovskite have not yet been studied. Therefore, the aim of this work was to investigate the effect of Sr deficiency on the conductivity of  $Sr_xZr_{0.95}Yb_{0.05}O_{3-\delta}$  ( $x = 0.94–1.00$ ) electrolytes.

## 2. Materials and Methods

$Sr_xZr_{0.95}Yb_{0.05}O_{3-\delta}$  ( $x = 0.94, 0.96, 0.98, 1.00$ ) powders were synthesized using  $ZrO(NO_3)_2 \cdot 2H_2O$ ,  $Yb(NO_3)_3 \cdot nH_2O$  and  $SrCO_3$  (all with 99% purity) as precursors via a chemical solution method. Solutions of zirconyl nitrate dehydrate in distilled water and ytterbium nitrate hydrate in ethanol, with concentrations of 62.9 g of  $ZrO_2$  and 24.4 g of  $Yb_2O_3$  per 1 L, respectively, were made. The solutions were mixed with  $SrCO_3$  powder in the ratios corresponding to the nominal compositions. Then, citric acid and glycine were added (the molar ratio of metal cations, glycine, and citric acid was 2:2:1). The solution was stirred and heated on a hot plate to evaporate the solvent until its ignition occurred, followed by calcining at a temperature of 1200 °C for 2 h. The obtained substance was reground into powder and pressed at 130 MPa. The pellets were then sintered in air at 1600 °C for 5 h.

The relative density of the sintered samples was determined by the Archimedes method using kerosene as a liquid. Crystal structure and phase composition of the obtained materials were investigated with the X-ray diffraction (XRD) method with  $Cu K\alpha$  radiation (D-Max 2200, Rigaku, Tokyo, Japan). Diffraction was carried out in the range from 10° to 90° at a scanning speed of 0.02°/min and step of 0.1°.

For the microstructure and composition study, the sintered pellets were polished, finishing with 1 µm grit diamond paste, and were thermally etched at a temperature of 1400 °C for 4 h to make the grain boundaries visible. The surface of the samples was studied using a MIRA 3 LMU (Tescan, Brno, Czech Republic) scanning electron microscope (SEM) equipped with an energy-dispersive X-ray spectroscopy (EDX) system (Oxford Instruments X-MAX 80, Abingdon, UK). For the chemical composition study, EDX data were collected and averaged for 10 spots.

Electrical conductivity of the samples was studied using two-probe AC impedance spectroscopy (Parstat 2273-SVS, Advanced Measurement Technology Inc., Oak Ridge, TN, USA) in a frequency range of 0.1 Hz–1 MHz with an amplitude of 30 mV. For the impedance measurements, platinum electrodes were applied to the pellets by painting Pt paste and were sintered at 1000 °C for 1 h in air. The surface area of the electrodes was 0.5 cm<sup>2</sup>, the

thickness of the pellets was 0.2 cm. The impedance measurements were carried out in the temperature range of 300–800 °C in air with controlled humidity. The water vapor partial pressure,  $p_{\text{H}_2\text{O}}$ , was held constant by passing the gas flow through a column filled with zeolites ( $p_{\text{H}_2\text{O}} = 0.04$  kPa) or through a water bubbler kept at 0 °C and 25 °C ( $p_{\text{H}_2\text{O}} = 0.61$  kPa and 3.2 kPa). Zview 2 software was used for the fittings of the measured Nyquist plots.

### 3. Results

#### 3.1. Microstructure, Phase and Chemical Composition of $\text{Sr}_x\text{Zr}_{0.95}\text{Yb}_{0.05}\text{O}_{3-\delta}$ Samples

XRD patterns of the obtained  $\text{Sr}_x\text{Zr}_{0.95}\text{Yb}_{0.05}\text{O}_{3-\delta}$  samples presented in Figure 1 were indexed on the basis of the  $\text{SrZrO}_3$  orthorhombic structure as confirmed by the corresponding ICDD file (44–0161). In the case of  $x \geq 0.96$ , no traces of minor phases were observed. For  $x = 0.94$ , except for the peaks of the major orthorhombic phase, two minor reflexes at 28° and 30.1° were recorded as can be clearly seen in Figure 1b. These reflexes were ascribed to  $\text{ZrO}_2$  monoclinic structure and Yb-stabilized  $\text{ZrO}_2$  cubic structure. Based on the XRD data, it can be concluded that the Sr-deficient homogeneity boundary in  $\text{Sr}_x\text{Zr}_{0.95}\text{Yb}_{0.05}\text{O}_{3-\delta}$  lays between  $x = 0.94$  and  $x = 0.96$ ; at the lower Sr contents,  $\text{ZrO}_2$ -based minor phases arise.

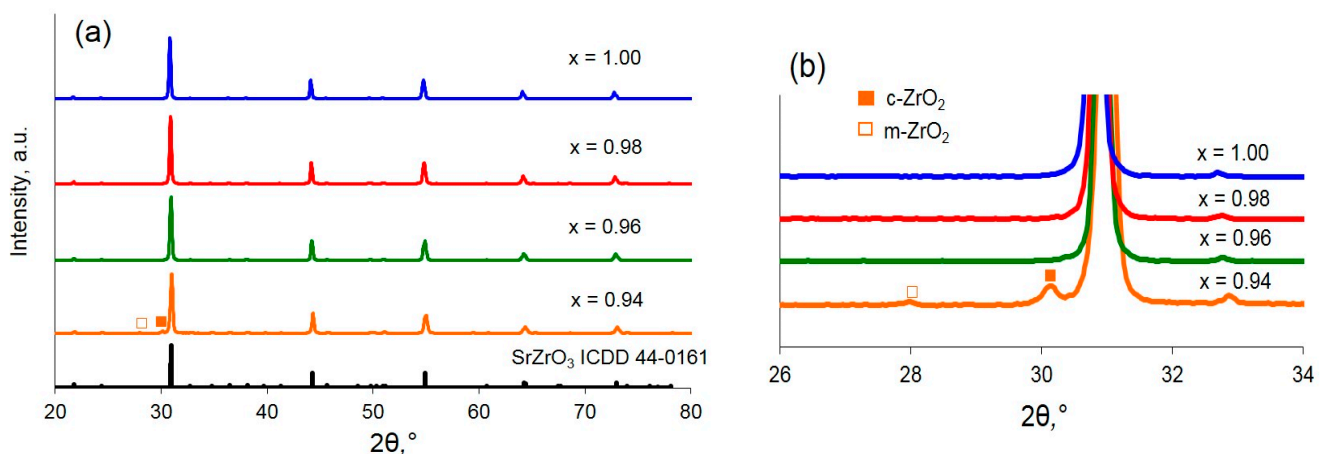


**Figure 1.** XRD patterns of the samples  $\text{Sr}_x\text{Zr}_{0.95}\text{Yb}_{0.05}\text{O}_{3-\delta}$ : (a) in the range of 20–80°, (b) enlarged XRD pattern between 26° and 34°.

The relative density of the sintered samples varied in the range of 90–95% with respect to the theoretical density. SEM images of the surface of  $\text{Sr}_x\text{Zr}_{0.95}\text{Yb}_{0.05}\text{O}_{3-\delta}$  samples shown in Figure 2a–c reveal dense microstructure with grains reaching 2.5  $\mu\text{m}$  in size. For the sample with the strongest Sr deficiency ( $x = 0.94$ ), the light grey grains with a diameter of 0.3–0.5  $\mu\text{m}$  embedded in the large grain matrix are observed. Figure 2d displays the fracture surface of the  $x = 0.94$  sample; the minor phase nanograins precipitated at the intergrain boundary can be clearly seen.

According to the EDX mapping images shown in Figure S1 and the measured element concentrations summarized in Table S1, the light grey grains observed in the SEM-image of the sample with  $x = 0.94$  contain mostly zirconium and ytterbium in the ratio close to 6:5. Taking into account the appearance of the X-ray reflection associated with the cubic  $\text{ZrO}_2$ -based phase, these grains can be considered as the precipitated phase of Yb-doped  $\text{ZrO}_2$ .

So, the obtained XRD, SEM and EDX data indicate that a decrease in the atomic concentration of strontium below 0.96 leads to nucleation of  $\text{ZrO}_2$ -based phases. Recently, the similar regularity was observed for the undoped and Y-doped  $\text{SrZrO}_3$  [19]. The process of the secondary phases' precipitation might be enhanced by the evaporation of strontium during the sintering of the ceramics. The surface alkaline earth metal depletion has been previously reported for the doped  $\text{SrZrO}_3$  and  $\text{BaZrO}_3$  ceramics [17,19,21,23] and explained by evaporation of the alkaline earth metals during the high-temperature treatment of ceramics.

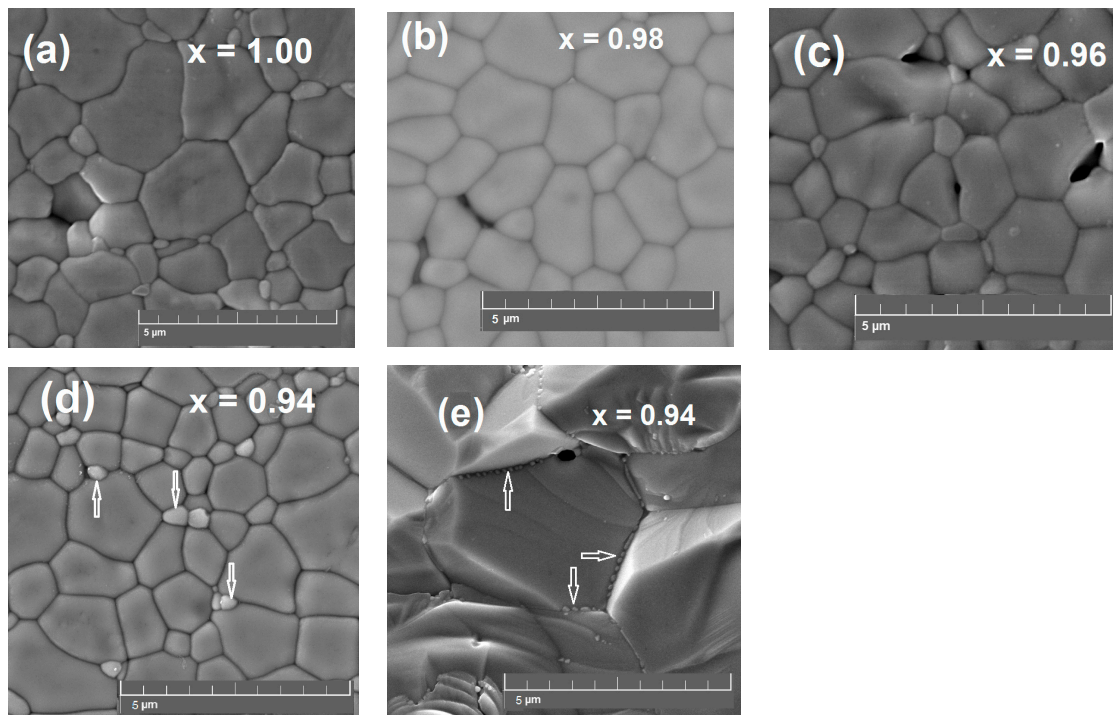


**Figure 2.** SEM images of  $\text{Sr}_x\text{Zr}_{0.95}\text{Yb}_{0.05}\text{O}_{3-\delta}$ : the surface of (a)  $x = 1.00$ , (b)  $0.98$ , (c)  $0.96$  and (d)  $0.94$  samples after polishing and thermal etching, (e) fracture of the  $x = 0.94$  sample. The impurity phase grains are marked with arrows.

### 3.2. Electrical Conductivity of $\text{Sr}_x\text{Zr}_{0.95}\text{Yb}_{0.05}\text{O}_{3-\delta}$

The electrical conductivity of the investigated samples was studied in the air with controlled humidity ( $p\text{H}_2\text{O} = 0.04, 0.61$  and  $3.2$  kPa) over the temperature range of  $300\text{--}800$  °C. To illustrate the influence of Sr content on the conduction features of  $\text{Sr}_x\text{Zr}_{0.95}\text{Yb}_{0.05}\text{O}_{3-\delta}$ , the impedance spectra of the samples with different Sr contents measured in dry ( $p\text{H}_2\text{O} = 0.04$  kPa) and wet ( $p\text{H}_2\text{O} = 3.2$  kPa) air at  $550$  °C are presented in Figure 3a,b. The hodographs measured at other temperatures and  $p\text{H}_2\text{O}$  are given in Figure S3. As can be seen, Sr deficiency has a significant impact on the shape of the hodographs. At the lowest Sr content ( $x = 0.94$ ), the total resistance increases by more than an order of magnitude, which is why the hodographs of this sample are shown in a separate plot (Figure 3c, S3m).

In dry air ( $p\text{H}_2\text{O} = 0.04$  kPa), the compositions with  $x = 0.98$  and  $1.00$  exhibit a semicircle with the characteristic capacitance of  $\sim 5\text{--}10^{-9}$   $\text{F cm}^{-2}$  at the characteristic frequency  $f_{\text{max}}$  (at maximum imaginary part of  $Z$ ) of  $\sim 20$  kHz and a small low-frequency arc ( $f_{\text{max}} \sim 5$  Hz) with a capacitance of  $10^{-5}$   $\text{F cm}^{-2}$  (Figure 3a). These spectra were deconvoluted with the help of the equivalent circuit shown in Figure S2a. Based on the obtained capacitance values, the high-frequency semicircle was ascribed to the grain boundary response. The high-frequency intersection of the semicircle with the real impedance axis was assigned to the bulk resistance of the electrolyte. At temperatures below  $550$  °C, a high-frequency arc with the characteristic capacitance of  $\sim 10^{-11}$   $\text{F cm}^{-2}$  starts to swell, which can be associated with the bulk response of the electrolyte; in these cases, the hodographs were described by the equivalent circuit presented in Figure S2b.

In contrast to  $x = 1.00$  and  $0.98$  samples, the Nyquist plot of the  $x = 0.96$  composition consists of three overlapping arcs at the characteristic frequencies of  $\sim 135$  kHz,  $\sim 5$  kHz and  $\sim 3$  Hz with the corresponding capacitances of  $\sim 10^{-9}$ ,  $10^{-8}$  and  $10^{-5}$   $\text{F cm}^{-2}$ . At lower temperatures in dry air ( $350$  °C,  $p\text{H}_2\text{O} = 0.04$  kPa), another high-frequency arc with the characteristic capacitance of  $\sim 10^{-11}$   $\text{F cm}^{-2}$  appears, which is apparently caused by the bulk response of the electrolyte (see Figure 3d and the equivalent circuit in Figure S2c). The low-frequency arc capacitance value ( $\sim 10^{-5}$   $\text{F cm}^{-2}$ ) is typical for the charge transfer

processes at the electrode/electrolyte interface; so, this arc was attributed to the interfacial contribution. The semicircles with the capacitances of  $\sim 10^{-9}$  and  $10^{-8}$  F cm $^{-2}$  can be associated with the grain boundary contribution and the precipitated minor phases response. As discussed above, the nominal Sr-deficiency and the evaporation losses initiate nucleation of ZrO $_2$ -based nanograins at the grain boundaries of the ceramic samples. We suppose that at  $x = 0.96$ , the minor phase contribution becomes visible on hodographs at medium frequency even though the impurities are not yet detectable by X-rays. The nanoscale size of the precipitated zirconia grains is responsible for the fact that their contribution is characterized by the capacitance of  $\sim 10^{-8}$  F cm $^{-2}$ , which is typical for grain boundaries.

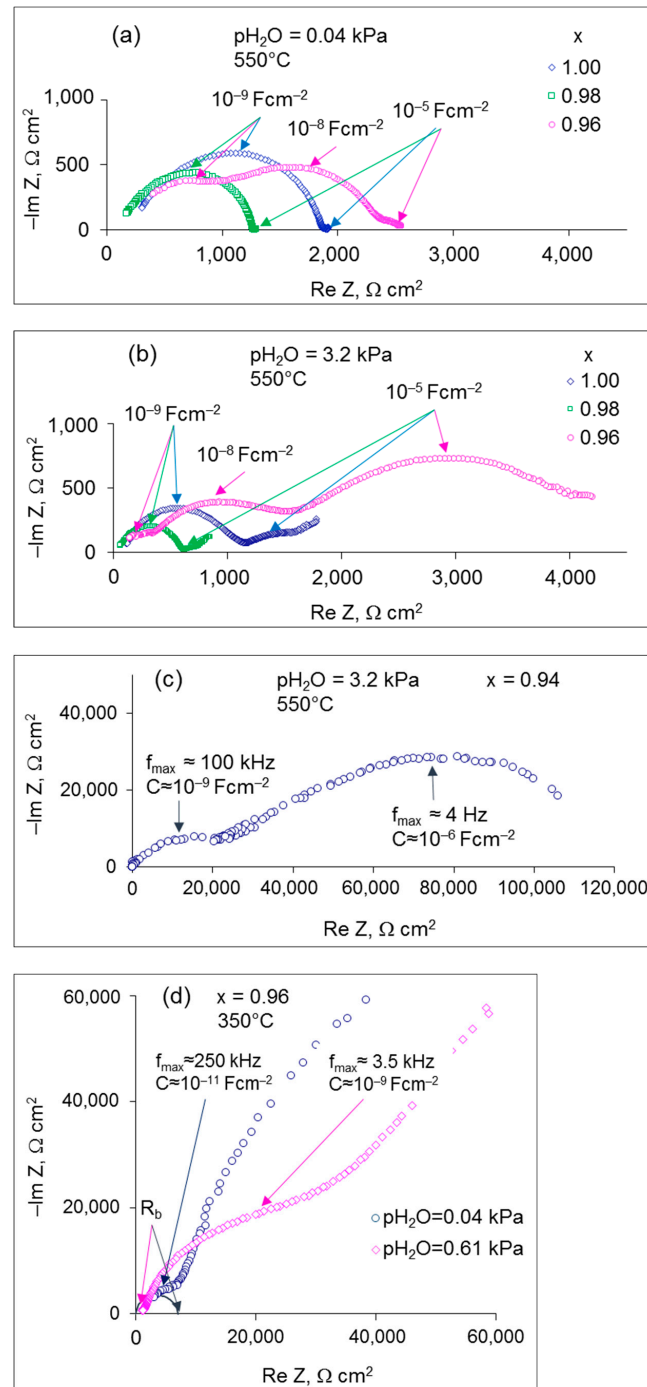


**Figure 3.** The impedance spectra for  $x = 0.96, 0.98$  and  $1.00$  samples measured at  $550^\circ\text{C}$  under (a)  $\text{pH}_2\text{O} = 0.04 \text{ kPa}$  and (b)  $3.2 \text{ kPa}$ ; (c)  $x = 0.94$ ,  $\text{pH}_2\text{O} = 3.2 \text{ kPa}$ ,  $550^\circ\text{C}$ ; (d) enlarged high-frequency fragments of the hodographs of the  $x = 0.96$  sample at  $350^\circ\text{C}$ .

The sample with  $x = 0.94$  exhibits a significantly larger impedance compared to other compositions as can be seen in Figure 3c. Two arcs with the characteristic capacitance of  $\sim 10^{-9} \text{ F cm}^{-2}$  and  $\sim 10^{-6} \text{ F cm}^{-2}$  can be distinguished on the hodograph measured under  $p\text{H}_2\text{O} = 3.2 \text{ kPa}$  at  $550^\circ\text{C}$ , which was deconvoluted with the help of the equivalent circuit shown in Figure S2d. The two arcs were assigned to the electrolyte response and the electrode polarization, respectively. A reliable deconvolution of the impedance spectra into the bulk and grain-boundary processes was not possible. Change of  $p\text{H}_2\text{O}$  had a weak effect on the shape of the impedance spectra of the  $x = 0.94$  sample.

To demonstrate the effect of humidity on the conducting properties of the  $x = 0.96\text{--}1.00$  samples, the Nyquist plots of the samples measured at different  $p\text{H}_2\text{O}$  values are depicted in Figure 4. With increasing  $p\text{H}_2\text{O}$ , both the bulk and grain boundary responses of the samples with  $x = 0.96\text{--}1.00$  shrink, which can be explained by the growing proton conduction; while the interfacial response with the characteristic capacitance of  $\sim 10^{-5} \text{ F cm}^{-2}$  significantly increases. Besides, a lower-frequency tail emerges in the spectra, which can be caused by slow gas diffusion through the porous electrodes.

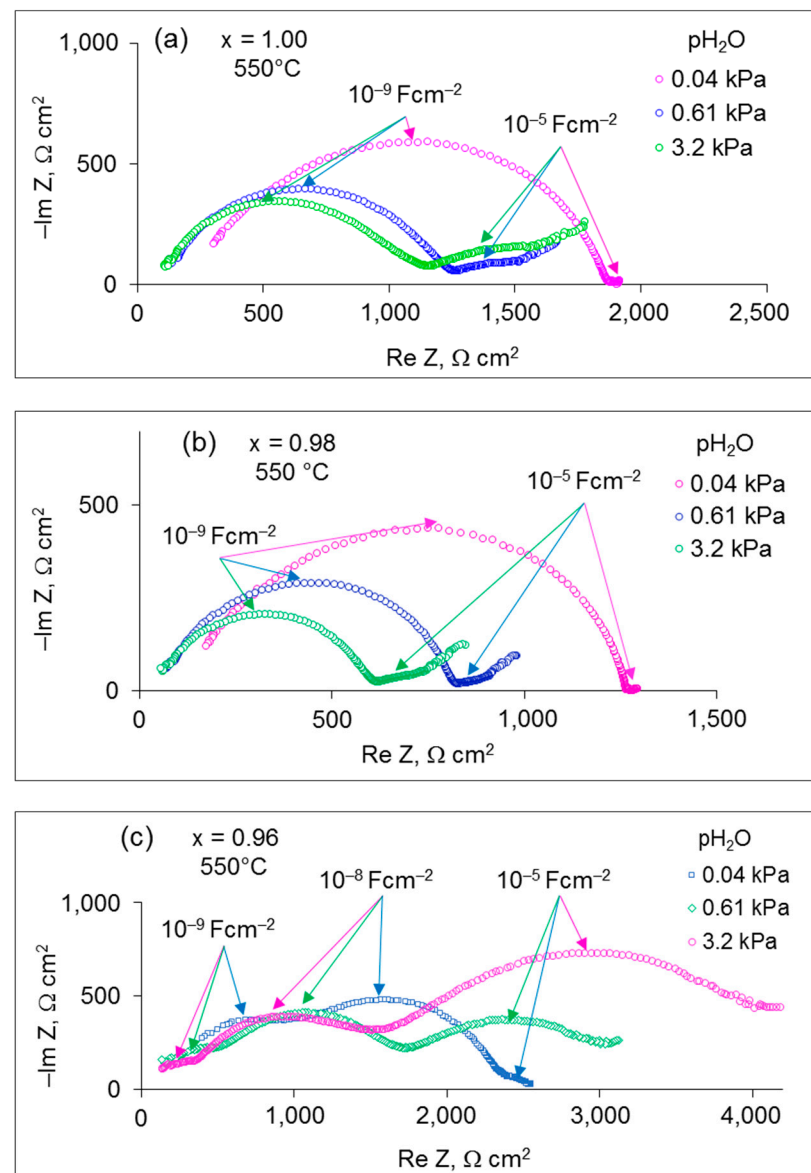


**Figure 4.** The impedance spectra for (a)  $x = 1.00$ , (b)  $x = 0.98$  and (c)  $x = 0.96$ , measured under different  $p\text{H}_2\text{O}$  at  $550^\circ\text{C}$ .

The total resistance  $R_t$  of the electrolyte is a sum of  $R_b$  and  $R_{gb}$  ( $R_b$  and  $R_{gb}$  denote the grain interior and grain boundary resistances). The grain interior, grain boundary and total conductivities were calculated using the obtained values of  $R_b$ ,  $R_{gb}$  and  $R_t$  by the following formula:

$$\sigma = L/SR, \quad (1)$$

where  $L$  denotes the sample thickness,  $S$  is the electrode area, and  $R$  is the related resistance.

Figure 5 displays the Arrhenius dependences of the total and bulk conductivities of  $\text{Sr}_x\text{Zr}_{0.95}\text{Yb}_{0.05}\text{O}_{3-\delta}$  samples. For all compositions, the conductivity of grain boundaries was close to the total conductivity, so it was not shown in order to avoid cluttering the figure. The total conductivities of all samples are linear in the Arrhenius plane in the whole investigated temperature range, while the grain interior conductivity dependences exhibit an inflection at  $\sim 600^\circ\text{C}$ . At temperatures above  $600^\circ\text{C}$ , the slopes of the bulk and total conductivity are similar, which means that the corresponding activation energies possess close values. Below the inflection point, the slope of the bulk conductivity decreases. Further, in the high temperature region (above  $600^\circ\text{C}$ ), the conductivity of grain bulk does not change with humidity, while at lower temperatures, it increases with a rise of  $\text{pH}_2\text{O}$  as can be seen in Figure 5. It is worth noting that the total conductivity of  $\text{Sr}_x\text{Zr}_{0.95}\text{Yb}_{0.05}\text{O}_{3-\delta}$  ( $x = 1.00$ ) obtained in the present research is similar to that of the same composition measured in air and reported in [22]. The literature data are presented in Figure 5a for comparison.

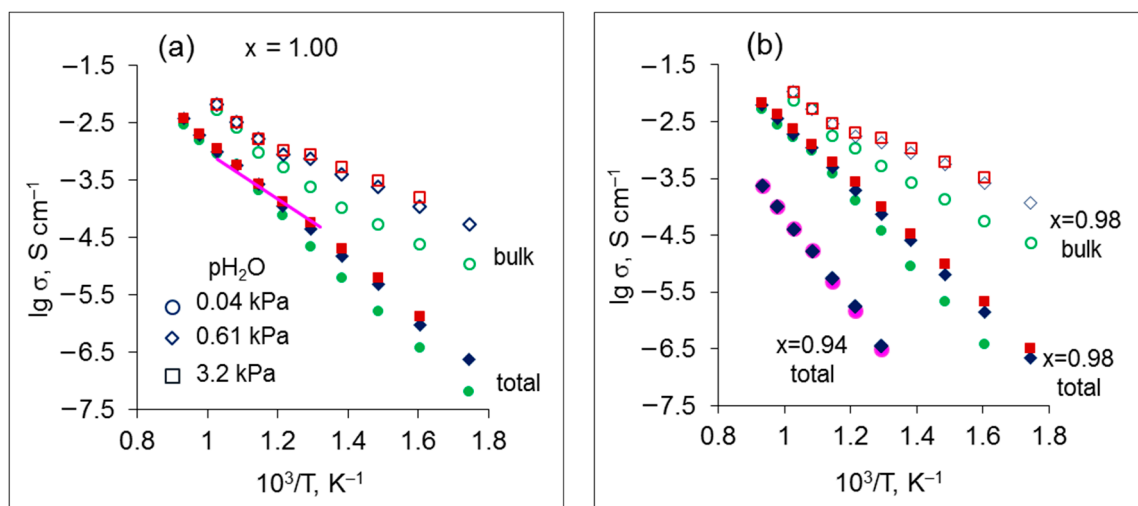


**Figure 5.** Arrhenius plots of the total and bulk conductivities of  $\text{Sr}_x\text{Zr}_{0.95}\text{Yb}_{0.05}\text{O}_{3-\delta}$  in air with different  $\text{pH}_2\text{O}$  values: (a)  $x = 1.00$ , (b)  $x = 0.94$  and  $0.98$ . Solid and open symbols denote total and bulk conductivity, respectively; circles, diamonds and squares correspond to  $\text{pH}_2\text{O} = 0.04$  kPa,  $0.61$  kPa and  $3.2$  kPa, respectively. A solid line represents the total conductivity of  $\text{SrZr}_{0.95}\text{Yb}_{0.05}\text{O}_{3-\delta}$  reported in [22].

The activation energies of the bulk and total conductivities of  $\text{Sr}_x\text{Zr}_{0.95}\text{Yb}_{0.05}\text{O}_{3-\delta}$  are summarized in Table 1. As can be seen, the activation energy of the bulk conductivity is sensitive to Sr deficiency and  $\text{pH}_2\text{O}$ : it decreases with decreasing  $x$  from  $1.00$  to  $0.96$  and with a rise of  $\text{pH}_2\text{O}$ . The effect of  $\text{pH}_2\text{O}$  can be explained by hydration of the samples and the appearance of protonic defects in humid atmospheres at relatively low temperatures. Water molecules incorporate into the lattice of  $\text{Sr}_x\text{Zr}_{0.95}\text{Yb}_{0.05}\text{O}_{3-\delta}$ , which results in the generation of protonic defects according to the following reaction:



where  $\text{O}_{\text{O}}^{\times}$  is an oxygen ion in a normal lattice site,  $\text{V}_{\text{O}}^{\cdot}$  is an oxygen vacancy,  $\text{OH}_{\text{O}}^{\cdot}$  denotes a proton localized on an oxygen ion, or a protonic defect.

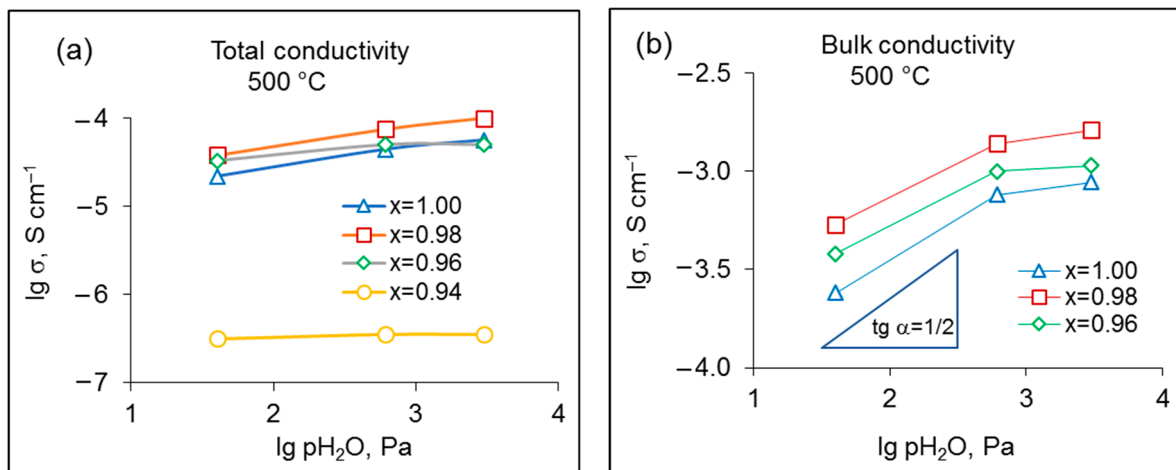
**Table 1.** Activation energies of the total and bulk conductivities of  $\text{Sr}_x\text{Zr}_{0.95}\text{Yb}_{0.05}\text{O}_{3-\delta}$ .

pH <sub>2</sub> O, kPa	E <sub>a, Tot</sub> , kJ mol <sup>-1</sup> (300–800 °C)			E <sub>a, Bulk</sub> , kJ mol <sup>-1</sup> (300–600 °C)	
	x = 0.96–1.00	x = 0.94	x = 1.00	x = 0.98	x = 0.96
0.04	112 ± 5		60 ± 2	58 ± 2	58 ± 2
0.61	98 ± 5	145 ± 8	49 ± 2	43 ± 2	39 ± 2
3.2	95 ± 5		45 ± 2	39 ± 2	32 ± 2

At low temperatures, Reaction (2) proceeds to the right to produce the protonic defects in the oxides. According to the law of mass action, the concentration of the bulk protonic defects increases proportionally to  $\text{pH}_2\text{O}^{1/2}$ . As temperature increases, the dehydration process progresses, with release of the proton defects from the oxide. So, in the low temperature range (below 600 °C), the bulk conductivity of the samples with  $x = 0.96$ – $1.00$  is mainly protonic, while at higher temperatures the contribution of protons in the charge transfer process decreases. Change of the dominant charge carriers causes the change of the bulk conductivity slope observed in the Arrhenius plots at  $\sim 600$  °C (see Figure 5).

The total conductivity behavior is restricted by grain boundaries; as a result, an increase in  $\text{pH}_2\text{O}$  leads to a slight decrease in the activation energy, whereas Sr content does not influence the activation energy of the total conductivity at  $x = 0.96$ – $1.00$ . As to the  $x = 0.94$  sample, the activation energy of the total conductivity is much higher than for other compositions and does not vary with a change of  $\text{pH}_2\text{O}$ , which indicates a negligibly small contribution of protons in the total conductivity.

Figure 6 shows the total and bulk conductivities of  $\text{Sr}_x\text{Zr}_{0.95}\text{Yb}_{0.05}\text{O}_{3-\delta}$  samples as functions of  $\text{pH}_2\text{O}$  at 500 °C in a logarithmic scale. The conductivity of the  $x = 0.96$ – $1.00$  samples increases with increasing  $\text{pH}_2\text{O}$ , which indicates the participation of protons in the process of charge transport. As can be seen in Figure 6b, at low humidity values, the slope of the bulk conductivity is close to  $\frac{1}{2}$ , being in agreement with Reaction (2); as the humidity increases, the slope decreases, which can be caused by saturation of the oxides with  $\text{H}_2\text{O}$ .

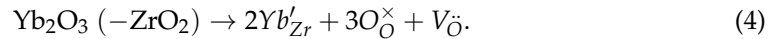
**Figure 6.** Total (a) and bulk (b) conductivity of  $\text{Sr}_x\text{Zr}_{0.95}\text{Yb}_{0.05}\text{O}_{3-\delta}$  samples as a function of  $\text{pH}_2\text{O}$  at 500 °C. Lines between points are only a guide to the eye.

Small deficiencies in Sr boost the conductivity of the strontium zirconate: the bulk conductivity of the  $x = 0.98$  composition is about 2.2 times more than that of  $x = 1.00$  over the studied  $\text{pH}_2\text{O}$  range. This can be explained by the increased oxygen vacancy concentration to maintain the charge neutrality according to the following reaction:

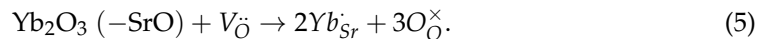


where  $V_{\text{Sr}}''$  is a vacancy of strontium.

The observed decline of the bulk conductivity upon further increase in Sr deficiency ( $x < 0.98$ ) can be caused by partitioning of  $\text{Yb}^{3+}$  ions over A- and B-sites in the doped  $\text{A}^{2+}\text{B}^{4+}\text{O}_3$  perovskite. Substitution of  $\text{Zr}^{4+}$  with  $\text{Yb}^{3+}$  results in a rise of the oxygen vacancy concentration according to Reaction (4), and thus, in an increase in the ionic conductivity:



However, incorporation of  $\text{Yb}^{3+}$  into  $\text{Sr}^{2+}$ -sites has the opposite effect on the oxygen vacancy concentration:



In Reactions (4) and (5),  $\text{Yb}'_{\text{Zr}}$  and  $\text{Yb}'_{\text{Sr}}$  denote the substitution defects in zirconium and strontium sites.

One can expect that the decreasing Sr concentration in  $\text{Sr}_x\text{Zr}_{0.95}\text{Yb}_{0.05}\text{O}_{3-\delta}$  disposes the placement of the dopant ions in A-sites. This trend was confirmed for the Sr-deficient zirconates doped with yttrium by Raman spectroscopy [23]. In this case, an increase in the Sr deficiency leads to a decrease in the ionic conductivity.

The total conductivity of  $\text{Sr}_x\text{Zr}_{0.95}\text{Yb}_{0.05}\text{O}_{3-\delta}$  is less sensitive to the Sr concentration because of the masking effect of grain boundaries (see Figure 6a). A sharp decrease in the total conductivity at  $x = 0.94$  can be explained by the nucleation and growth of the minor zirconia-based phases including the poorly conducting monoclinic zirconia, which hinders the transport of oxide ions and protonic defects.

The data on the influence of the Sr deficiency on the electrical conductivity of Yb-doped strontium zirconate obtained in the present research show the importance of controlling the concentration of the alkaline earth elements in zirconates. As was mentioned above, SrO evaporates during sintering of the ceramics, which can lead to deviations from the stoichiometry and an undesirable increase in the electrolyte resistance.

It is of importance to consider the influence of  $\text{pH}_2\text{O}$  on the electrode behavior. As can be seen from the impedance spectra (Figures 3 and 4), the interfacial polarization rises with increasing  $\text{pH}_2\text{O}$ , which can be explained by suppressing the hole conductivity because of the incorporation of water molecules into the solid oxide lattice [24]. In dry oxidizing atmospheres, the interaction of the oxides with oxygen results in the generation of electron holes as described by the following reaction:



The presence of electron holes facilitates the charge transfer reactions at the electrode/electrolyte interface. In humid air, the incorporation of water (Reaction (2)) competes with that of oxygen (Reaction (6)), which leads to a decrease in the hole concentration; as a result, the interfacial polarization increases as  $\text{pH}_2\text{O}$  rises. In the high temperature range, dehydration of the materials causes the hole concentration to increase, which alleviates the electrode polarization. Indeed, the polarization resistance of the studied cells was nearly independent of humidity at high temperatures (750–800 °C).

Recently, we reported the conductivity of the  $\text{Sr}_x\text{Zr}_{0.95}\text{Y}_{0.05}\text{O}_{3-\delta}$  series ( $x = 0.94\text{--}1.02$ ) [19]. It is worth comparing the influence of the dopant type on the transport properties of the zirconates. In both yttrium and ytterbium doping, the Sr-deficient compositions ( $x = 0.98$ ) exhibits the highest conductivity. The bulk conductivity of  $\text{Sr}_{0.98}\text{Zr}_{0.95}\text{Yb}_{0.05}\text{O}_{3-\delta}$  is about ten times higher than that of  $\text{Sr}_{0.98}\text{Zr}_{0.95}\text{Y}_{0.05}\text{O}_{3-\delta}$ . This can be explained by a larger number of the electron shells in ytterbium and the greater shielding effect experienced by the ionic charge carriers ( $\text{V}_\text{O}^\bullet$  and  $\text{OH}_\text{O}^\bullet$ ), which provides the higher charge carriers mobility. Therefore, doping with Yb is preferable to raising the conductivity.

#### 4. Conclusions

The effect of Sr stoichiometry on microstructure, phase composition and electrical conductivity of  $\text{Sr}_x\text{Zr}_{0.95}\text{Yb}_{0.05}\text{O}_{3-\delta}$  ( $x = 0.94\text{--}1.00$ ) was investigated via XRD, SEM, EDX and impedance spectroscopy. The samples were synthesized by the chemical solution method using  $\text{ZrO}(\text{NO}_3)_2 \cdot 2\text{H}_2\text{O}$ ,  $\text{Yb}(\text{NO}_3)_3 \cdot n\text{H}_2\text{O}$  and  $\text{SrCO}_3$  as precursors, and sintered at  $1600\text{ }^\circ\text{C}$ , 5 h. The  $x = 0.96\text{--}1.00$  samples were shown to be single-phase; the further increase of Sr-deficiency promoted the nucleation process of zirconia-based phases.

Small Sr deficiency was shown to improve the conductivity due to the formation of additional oxygen vacancies; as a result, the  $x = 0.98$  composition exhibited the highest total and bulk conductivity, which reached  $6\text{--}10^{-4}\text{ Scm}^{-1}$  and  $3 \cdot 10^{-3}\text{ Scm}^{-1}$  at  $600\text{ }^\circ\text{C}$  in wet air ( $p\text{H}_2\text{O} = 3.2\text{ kPa}$ ). A decrease in the conductivity at stronger Sr deficiencies can be explained by the partitioning of the dopant ions ( $\text{Yb}^{3+}$ ) over A- and B-sites in the doped  $\text{A}^{2+}\text{B}^{4+}\text{O}_3$  perovskite and the related decrease in the oxygen vacancy concentration. A sharp decrease in the total conductivity at  $x = 0.94$  was explained by the nucleation of the minor zirconia-based phases including the poorly conducting monoclinic zirconia. The conductivity of the samples with  $x = 0.96\text{--}1.00$  increased with the increase in humidity in the temperature range of  $300\text{--}600\text{ }^\circ\text{C}$ , which indicates a notable contribution of protons to the charge transport. The conductivity of Yb-doped strontium zirconate exceeds that of Y-doped zirconate, which makes it a more prospective material for application in PC-SOFCs.

**Supplementary Materials:** The following supporting information can be downloaded at: <https://www.mdpi.com/article/10.3390/ma15124126/s1>, Figure S1: (a) Back scattered electron image of  $x = 0.94$  sample and (b) corresponding EDX mapping images of Sr, Zr, Yb and O; Figure S2: Equivalent circuits used for deconvolution of impedance spectra for: (a)  $x = 0.98$  and  $1.00$  at  $550\text{--}800\text{ }^\circ\text{C}$ ; (b)  $x = 0.98$  and  $1.00$  at  $500\text{ }^\circ\text{C}$  and below; (c)  $x = 0.96$  at  $350\text{ }^\circ\text{C}$  and below; (d)  $x = 0.94$ .  $R_t$  denotes the total resistance of a sample;  $R_b$ ,  $R_{gb}$ ,  $R_{mp}$  and  $R_e$  are the grain interior, grain boundary, minor phase and electrode resistances, respectively;  $Q_b$ ,  $Q_{gb}$ ,  $Q_{mp}$  and  $Q_e$  are the constant phase element associated with the grain interior, grain boundary, minor phase and electrode responses;  $Q_t$  is the constant phase element related with the total re-sponse of a sample; Figure S3: Impedance spectra of the samples with  $x = 0.96\text{--}1.00$  measured in air at  $700\text{ }^\circ\text{C}$  (a–c),  $600\text{ }^\circ\text{C}$  (d–f),  $500\text{ }^\circ\text{C}$  (g–i) and  $400\text{ }^\circ\text{C}$  (j,k); at  $p\text{H}_2\text{O} = 0.04\text{ kPa}$  (a,d,g,j),  $0.61\text{ kPa}$  (b,e,h,k) and  $3.2\text{ kPa}$  (c,f,i); and the spectra of the  $x = 0.94$  sample at  $p\text{H}_2\text{O} = 0.04\text{ kPa}$  (l); Table S1: Elemental composition (at.%) of the surface of  $x = 0.94$  sample after polishing and thermal etching ( $1400\text{ }^\circ\text{C}$ , 4 h) from EDX data.

**Author Contributions:** Conceptualization, methodology, supervision, writing—review and editing, L.D.; sample preparation, A.M. and A.K.; investigation, data curation, A.K., A.M. and A.P.; visualization, writing—original draft preparation, A.K. All authors have read and agreed to the published version of the manuscript.

**Funding:** This research received no external funding.

**Institutional Review Board Statement:** Not applicable.

**Informed Consent Statement:** Not applicable.

**Data Availability Statement:** Not applicable.

**Acknowledgments:** SEM, EDX and XRD experiments were done using facilities of the shared access center “Composition of compounds” (Institute of High Temperature Electrochemistry, Ural Branch of the Russian Academy of Sciences).

**Conflicts of Interest:** The authors declare no conflict of interest.

#### References

1. Duan, C.; Huang, J.; Sullivan, N.; O’Hayre, R. Proton-conducting oxides for energy conversion and storage. *Appl. Phys. Rev.* **2020**, *7*, 011314. [CrossRef]
2. Loureiro, F.J.A.; Perez-Coll, D.; Graça, V.C.D.; Mikhalev, S.M.; Ribeiro, A.F.G.; Mendes, A.; Fagg, D.P. Proton conductivity in yttrium-doped barium cerate under nominally dry reducing conditions for application in chemical synthesis. *J. Mater. Chem. A* **2019**, *7*, 18135–18142. [CrossRef]

3. Han, D.; Liu, X.; Bjørheim, T.S.; Uda, T. Yttrium-Doped Barium Zirconate-Cerate Solid Solution as Proton Conducting Electrolyte: Why Higher Cerium Concentration Leads to Better Performance for Fuel Cells and Electrolysis Cells. *Adv. Energy Mater.* **2021**, *11*, 2003149. [\[CrossRef\]](#)
4. Iwahara, H.; Yajima, T.; Hibino, T.; Ozaki, K.; Suzuki, H. Protonic conduction in calcium, strontium and barium zirconates. *Solid State Ion.* **1993**, *61*, 65–69. [\[CrossRef\]](#)
5. Yajima, T.; Suzuki, H.; Yogo, T.; Iwahara, H. Protonic conduction in SrZrO<sub>3</sub>-based oxides. *Solid State Ion.* **1992**, *51*, 101–107. [\[CrossRef\]](#)
6. Higuchi, T.; Tsukamoto, T.; Sata, N.; Hiramoto, K.; Ishigame, M.; Shin, S. Protonic conduction in the single crystals of SrZr<sub>0.95</sub>M<sub>0.05</sub>O<sub>3</sub> (M = Y, Sc, Yb, Er). *Jpn. J. Appl. Phys.* **2001**, *40*, 4162–4163. [\[CrossRef\]](#)
7. Zhang, W.; Hang, H.Y. Progress in proton-conducting oxides as electrolytes for low-temperature solid oxide fuel cells: From materials to devices. *Energy Sci. Eng.* **2021**, *9*, 984–1011. [\[CrossRef\]](#)
8. Zając, W.; Rusinek, D.; Zheng, K.; Molenda, J. Applicability of Gd-doped BaZrO<sub>3</sub>, SrZrO<sub>3</sub>, BaCeO<sub>3</sub> and SrCeO<sub>3</sub> proton conducting perovskites as electrolytes for solid oxide fuel cells. *Cent. Eur. J. Chem.* **2013**, *11*, 471–484. [\[CrossRef\]](#)
9. Holz, L.I.V.; Graça, V.C.D.; Loureiro, F.J.A.; Fagg, D.P. *Analytical Chemistry—Advancement, Perspectives and Applications*; Srivastava, A.N., Ed.; IntechOpen Limited: London, UK, 2020; Volume 3, p. 248. [\[CrossRef\]](#)
10. Jhuang, J.-W.; Lee, K.-R.; Chang, J.-K.; Shen, C.-T.; Lee, Y.-H.; Lee, S.-W.; Tseng, C.-J. Chemical stability and electrical and mechanical properties of BaZr<sub>x</sub>Ce<sub>0.8-x</sub>Y<sub>0.2</sub>O<sub>3</sub> with CeO<sub>2</sub> protection method. *Int. J. Hydrogen Energy* **2017**, *42*, 22259–22265. [\[CrossRef\]](#)
11. Li, S.; Irvine, J.T.S. Non-stoichiometry, structure and properties of proton-conducting perovskite oxides. *Solid State Ion.* **2021**, *361*, 115571. [\[CrossRef\]](#)
12. Krug, F.; Schober, T. The high-temperature proton conductor strontium zirconate: Thermogravimetry of water uptake. *J. Am. Ceram. Soc.* **1997**, *80*, 794–796. [\[CrossRef\]](#)
13. Yamazaki, Y.; Babilo, P.; Haile, S.M. Defect Chemistry of Yttrium-Doped Barium Zirconate: A Thermodynamic Analysis of Water Uptake. *Chem. Mater.* **2008**, *20*, 6352–6357. [\[CrossRef\]](#)
14. Hossain, M.K.; Tamura, H.; Hashizume, K. Visualization of hydrogen isotope distribution in yttrium and cobalt doped barium zirconates. *J. Nucl. Mater.* **2020**, *538*, 152207. [\[CrossRef\]](#)
15. Hossain, M.K.; Hashizume, K.; Hatano, Y. Evaluation of the hydrogen solubility and diffusivity in proton-conducting oxides by converting the PSL values of a tritium imaging plate. *Nucl. Mater. Energy* **2020**, *25*, 100875. [\[CrossRef\]](#)
16. Mukundan, R.; Brosha, E.L.; Birdsell, S.A.; Costello, A.L.; Garzon, F.H.; Willms, R.S. Tritium Conductivity and Isotope Effect in Proton-Conducting Perovskites. *J. Electrochem. Soc.* **1999**, *146*, 2184–2187. [\[CrossRef\]](#)
17. Yamazaki, Y.; Hernandez-Sanchez, R.; Haile, S.M. Cation non-stoichiometry in yttrium-doped barium zirconate: Phase behavior, microstructure, and proton conductivity. *J. Mater. Chem.* **2010**, *20*, 8158–8166. [\[CrossRef\]](#)
18. Weston, L.; Janotti, A.; Cui, X.Y.; Stampfl, C.; Van de Walle, C.G. Acceptor doping in the proton conductor SrZrO<sub>3</sub>. *Phys. Chem. Chem. Phys.* **2017**, *19*, 11485–11491. [\[CrossRef\]](#)
19. Dunyushkina, L.A.; Khaliullina, A.S.; Meshcherskikh, A.N.; Pankratov, A.A.; Osinkin, D.A. Effect of A-site nonstoichiometry on defect chemistry and electrical conductivity of undoped and Y-doped SrZrO<sub>3</sub>. *Materials* **2019**, *12*, 1258. [\[CrossRef\]](#)
20. Sharova, N.V.; Gorelov, V.P. Effect of Cation Nonstoichiometry on the Properties of Solid Electrolyte Ba<sub>x</sub>Ce<sub>0.97</sub>Nd<sub>0.03</sub>O<sub>3-d</sub> (0.90 ≤ x ≤ 1.10). *Russ. J. Electrochem.* **2004**, *40*, 639–645. [\[CrossRef\]](#)
21. Yang, W.; Zhou, H.; Wang, L.; Li, Y.; He, Z.; Han, C.; Dai, L. The influence of Ba-site non-stoichiometry on the phase composition, sinterability, conductivity and chemical stability of Ba<sub>x</sub>Zr<sub>0.6</sub>Hf<sub>0.2</sub>Y<sub>0.2</sub>O<sub>3-d</sub> (0.9 ≤ x ≤ 1.03) proton conductors. *Int. J. Hydrogen Energy* **2021**, *46*, 10838–10849. [\[CrossRef\]](#)
22. Bootharajan, M.; Rao, J.S.B.; Kumar, R.; Jayaraman, V. Behavior of Ytterbium in Calcium and Strontium Zirconate Matrices. *ECS J. Solid State Sci. Technol.* **2017**, *6*, N10–N16. [\[CrossRef\]](#)
23. Shkerin, S.N.; Rudakova, A.V.; Bulanin, K.M.; Khaliullina, A.S.; Meshcherskikh, A.N.; Vovkotrub, E.G.; Dunyushkina, L.A. Raman spectroscopy of SrZrO<sub>3</sub> based proton conducting electrolyte: Effect of Y-doping and Sr-nonstoichiometry. *Int. J. Hydrogen Energy* **2021**, *46*, 17007–17018. [\[CrossRef\]](#)
24. Taherparvar, H.; Kilner, J.A.; Baker, R.T.; Sahibzada, M. Effect of Humidification at Anode and Cathode in Proton-Conducting SOFCs. *Solid State Ion.* **2003**, *162–163*, 297–303. [\[CrossRef\]](#)